



**HAL**  
open science

## Ellipsometry Study of Hexagonal Boron Nitride using Synchrotron Radiation: Transparency Window in the Far-UVC

Luis Artús, Martin Feneberg, Claudio Attaccalite, James H Edgar, Jiahan Li, Rüdiger Goldhahn, Ramon Cuscó

► **To cite this version:**

Luis Artús, Martin Feneberg, Claudio Attaccalite, James H Edgar, Jiahan Li, et al.. Ellipsometry Study of Hexagonal Boron Nitride using Synchrotron Radiation: Transparency Window in the Far-UVC. *Advanced Photonics Research*, 2021, pp.2000101. 10.1002/adpr.202000101 . hal-03142453

**HAL Id: hal-03142453**

**<https://hal.science/hal-03142453>**

Submitted on 9 Nov 2021

**HAL** is a multi-disciplinary open access archive for the deposit and dissemination of scientific research documents, whether they are published or not. The documents may come from teaching and research institutions in France or abroad, or from public or private research centers.

L'archive ouverte pluridisciplinaire **HAL**, est destinée au dépôt et à la diffusion de documents scientifiques de niveau recherche, publiés ou non, émanant des établissements d'enseignement et de recherche français ou étrangers, des laboratoires publics ou privés.



Distributed under a Creative Commons Attribution 4.0 International License

# Ellipsometry Study of Hexagonal Boron Nitride Using Synchrotron Radiation: Transparency Window in the Far-UVC

Luis Artús,\* Martin Feneberg, Claudio Attacalite, James H. Edgar, Jiahan Li, Rüdiger Goldhahn, and Ramon Cuscó

The linear optical response of the ultrawide bandgap *h*-BN is investigated by spectroscopic ellipsometry. The ordinary dielectric function of *h*-BN is determined up to 25 eV on a high-quality single-crystal platelet. The direct bandgap and the high-energy transitions are characterized with the aid of ab initio self-consistent *GW* calculations and the optical properties are calculated using the Bethe–Salpeter equation. The dispersion of the ordinary refractive index in the visible and UV part of the spectrum below the bandgap is in excellent agreement with previous transmission experiments. A sharp excitonic peak at 6.1 eV associated with the direct bandgap dominates the absorption spectrum, and a second peak is observed at 6.8 eV. At higher energies, a strong absorption peak emerges at 15 eV associated with higher  $\sigma \rightarrow \sigma^*$  transitions. As a consequence of the unique electronic band structure of *h*-BN, a transparency window is observed in the far-UV region between 7 and 13 eV, where the light penetration depth reaches a value of 38 nm, as opposed to the value of 0.8 nm at the absorption peak of the fundamental bandgap.

## 1. Introduction

Ultrahigh bandgap semiconductors are central to a wide range of innovative applications such as disinfection systems, water purification, biochemical sensing, photo catalysis, solar-blind detection, and non-line-of-sight communication.<sup>[1–6]</sup> The development of deep-UV (UVC) light-emitting diodes (LEDs) is attracting an enormous research effort, as they are emerging as a promising

replacement of UVC gas discharge lamps that will enable a mercury-free, cheap and accessible sterilization technology capable to face present-day needs for portable disinfection systems and germicidal water treatment.<sup>[1,7]</sup> While the UVC spans the spectral region between 100 and 280 nm (ISO 21348),<sup>[8]</sup> the far-UVC region below 200 nm is of particular interest in this respect. Far-UVC light irradiation has been proven to inactivate airborne human coronavirus whereas, due to its small penetration range in biological tissues, does not reach living cells in the skin or eyes, thus avoiding hazards associated with conventional UV light.<sup>[9,10]</sup> The far-UVC region is accessible by a range of excimer lamps, most notably the 172 nm Xe<sub>2</sub> lamp.<sup>[11]</sup> This highly energetic radiation finds other numerous applications in a wide range of fields, such as waste treatment and water photolysis,<sup>[12–14]</sup> photopolymerization curing of nanocomposite coatings,<sup>[15]</sup> and high-resolution lithography.<sup>[16]</sup>

The tremendous success of InGaN-based LEDs<sup>[17]</sup> has stimulated the research on the AlGaN nitride alloy system to extend the wavelength range to the deep-UV.<sup>[18]</sup> However, widespread use of AlGaN LEDs is severely limited by their low light extraction efficiency.<sup>[19]</sup> Moreover, the relatively thick AlGaN layers with high Al concentration required for laser diode operation result

Prof. L. Artús, Dr. R. Cuscó  
Geo3Bcn-CSIC  
Consejo Superior de Investigaciones Científicas  
Lluís Solé i Sabarís s.n., Barcelona 08028, Spain  
E-mail: lartus@geo3bcn.csic.es

Dr. M. Feneberg  
Institut für Physik  
Otto-von-Guericke-Universität Magdeburg  
Universitätsplatz 2, 39106 Magdeburg, Germany

 The ORCID identification number(s) for the author(s) of this article can be found under <https://doi.org/10.1002/adpr.202000101>.

© 2021 The Authors. Advanced Photonics Research published by Wiley-VCH GmbH. This is an open access article under the terms of the Creative Commons Attribution License, which permits use, distribution and reproduction in any medium, provided the original work is properly cited.

Dr. C. Attacalite  
Aix Marseille University  
CNRS  
Centre Interdisciplinaire de Nanoscience de Marseille UMR 7325  
Campus de Luminy Case 913, Marseille 13288, France

Prof. J. H. Edgar, Dr. J. Li  
Tim Taylor Department of Chemical Engineering  
Kansas State University  
Manhattan, KS 66506, USA

Prof. R. Goldhahn  
Institut für Physik  
Otto-von-Guericke-Universität Magdeburg  
Universitätsplatz 2, 39106 Magdeburg, Germany

DOI: 10.1002/adpr.202000101

in high dislocation densities and a significant degradation of the internal quantum efficiency. To circumvent these drawbacks, advancements in the design of deep-UV LEDs using AlN substrates with very low dislocation densities are currently being actively investigated.<sup>[20,21]</sup> On the other hand, direct wide bandgap oxides have also aroused a notable interest for the realization of future UV applications.<sup>[22]</sup> In particular, considerable efforts are being devoted to develop Ga<sub>2</sub>O<sub>3</sub>-based devices.<sup>[23]</sup> Nevertheless, because of the relatively low bandgap of the most stable  $\beta$ -Ga<sub>2</sub>O<sub>3</sub> phase (reported in the 4.6–4.9 eV range),<sup>[22]</sup> this material is not a real contender for applications in the UVC region. A higher bandgap of  $\approx$ 5.6 eV has been reported for the metastable  $\alpha$ -Ga<sub>2</sub>O<sub>3</sub> phase.<sup>[24,25]</sup>

After the seminal paper by Watanabe et al.,<sup>[26]</sup> which demonstrated UV lasing at 215 nm in *h*-BN single crystal grown under high-pressure and high-temperature conditions, a new competitor to AlN has emerged in the area of semiconductor materials for UVC applications. The first *h*-BN-based electroluminescent device in the deep-UV range was soon later realized.<sup>[27]</sup> The remarkable properties of *h*-BN have stimulated a great deal of research and have established *h*-BN as a promising material for a wide range of applications, including infrared nanophotonics, quantum photonics, nonlinear optics, and deep-UV optoelectronics,<sup>[28]</sup> in addition to applications in nanocomposite ceramics for multifunctional biomaterials.<sup>[29]</sup> Strong Coulomb interactions in *h*-BN lend excitonic effects a major role in determining the electronic structure and the optical response of *h*-BN.<sup>[30–32]</sup> The physical mechanisms leading to the bright UV emission of *h*-BN have been object of debate. While Watanabe et al. attributed the *h*-BN luminescence to direct excitonic recombinations,<sup>[26]</sup> all-electron quasiparticle calculations indicated an indirect gap.<sup>[30]</sup> More recent experiments have identified the emission lines of *h*-BN as phonon-assisted recombination from an indirect excitonic transition.<sup>[33]</sup> The phonon-assisted luminescence of bulk *h*-BN exhibits a surprisingly high quantum yield that is comparable with that of direct bandgap semiconductors. The role of phonons at the *T* point of the Brillouin zone and of the shear mode overtones at zone center in the optical emission of *h*-BN was thoroughly investigated.<sup>[34]</sup> Recently, a substantial amount of theoretical work has been devoted to the calculation of phonon-assisted luminescence and optical absorption spectra in *h*-BN to elucidate the long-debated Stokes shift.<sup>[31,35,36]</sup> The relevance of phonons in *h*-BN emission and in phonon-polariton hybrid excitations<sup>[37,38]</sup> has inspired a fair amount of detailed optical studies of the *h*-BN phonons by means of Raman scattering<sup>[39–43]</sup> and infrared transmission/reflexivity measurements.<sup>[44–46]</sup>

While *ab initio* calculations of the optical properties and quasiparticle electronic band structure of *h*-BN in the GW approximation have been available for some time,<sup>[30,32,47]</sup> experimental studies probing the optical excitations of *h*-BN are very scarce. Spectroscopic ellipsometry is an extremely sensitive tool to study the linear optical response of materials that can provide an accurate determination of the interband transitions in layered compounds. Kravets et al.<sup>[48]</sup> reported near-UV absorption in graphene layers using spectroscopic ellipsometry. Spectroscopic ellipsometry measurements were also used to reveal the predominant *sp*<sup>2</sup> or *sp*<sup>3</sup> character of BN films prepared by magnetron sputtering.<sup>[49]</sup> Recently, the ellipsometric technique has been

applied to characterize the crystalline quality of *h*-BN samples with the presence of turbostratic layers,<sup>[50]</sup> but a comprehensive ellipsometric study on *h*-BN giving insight into the optical properties is still lacking. Ellipsometry measurements allow the dielectric function of *h*-BN to be determined without the need of performing the Kramers–Kronig analysis that is necessary in the case of reflectance and absorption measurements.

In this work, we present a spectroscopic ellipsometric study of high-quality single-crystal *h*-BN for energies up to 25 eV using synchrotron radiation. To the best of our knowledge, these are the first ellipsometric measurements performed on a van der Waals crystal using synchrotron light. The ordinary dielectric function is determined and the most salient features are identified with the aid of *ab initio* calculations. The excitonic transitions of the quasiparticle band structure calculated in the GW approximation are in good agreement with the peaks in the imaginary part of the dielectric function. Remarkably, unlike high-bandgap materials which are opaque in the far-UVC, *h*-BN exhibits a wide transparency window beyond the fundamental direct bandgap energy. While well-established far-UV optical materials such as CaF<sub>2</sub> or BaF<sub>2</sub> offer a superior transmission at the ArF excimer laser emission (193 nm),<sup>[51]</sup> the region where the laminar *h*-BN material exhibits above-bandgap transmission extends to 95 nm. This fact, together with the fact that *h*-BN exhibits an exceptionally good thermal conductivity and can be integrated in 2D devices, could be exploited in future far-UVC technological applications.

## 2. Results and Discussion

The complex ordinary dielectric function of *h*-BN is shown in **Figure 1** for energies from 0.5 up to 25 eV. The red curves correspond to the point-by-point fits to the ellipsometric data, and they reveal a dominant transition at 6.12 eV followed by weaker but clearly visible one at 6.82 eV. A strong broader peak can be seen at 14.96 eV and a weaker band centered at about 19.2 eV can also be observed. The first transition corresponds to an excitonic absorption of the direct bandgap and marks the onset of strong absorption. Although bulk *h*-BN is an indirect insulator, indirect transitions are not observed in optical spectra because their intensity is expected to be much lower compared with the main exciton peak.<sup>[31,35]</sup> Moreover, due to the band structure of *h*-BN, the indirect excitonic transitions yield absorption peaks very close to the direct transition, making it impossible to distinguish indirect contributions to absorption.<sup>[36]</sup>

In the energy range below 6 eV, the dispersion of the refractive index was previously determined from optical transmittance experiments.<sup>[44]</sup> Those measurements revealed a giant anisotropy in the refractive index and a steep increase in the ordinary refractive index  $n_{\perp}$  as the bandgap energy is approached,<sup>[44]</sup> which was ascribed to strong excitonic effects close to the bandgap. As shown in **Figure 2**, the ellipsometric determination of  $n_{\perp}$  shows a remarkably good agreement with transmission optical interference data. The ellipsometry data show a steep increase in  $n_{\perp}$  from around 2.3 in the near-IR–visible region up to 3.7 close to the fundamental bandgap. In this transparency region, the ordinary refractive index is accurately described by the rational polynomial  $n_{\perp}(E) = (a_0 + a_1 E)/(E - a_2)$ , where  $a_0 = -14.39$  eV,  $a_1 = 2.05$ ,

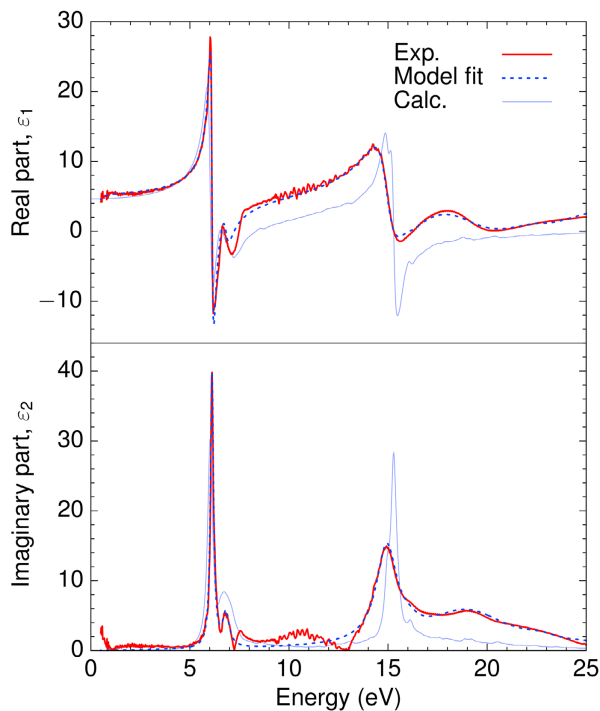


**Figure 1.** Real (upper panel) and imaginary (lower panel) ordinary dielectric functions of *h*-BN. The dotted lines represent model fits to the data. The point-by-point fits to the experimental ellipsometric data (red lines) are compared with the results of ab initio calculations (light blue curves).

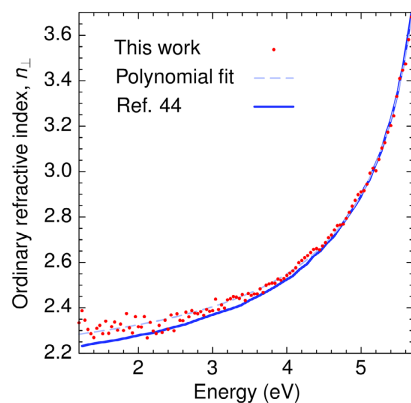


**Figure 2.** Below-bandgap ordinary refractive index of *h*-BN derived from ellipsometric measurements compared with previous optical transmittance determination. The dashed line is a rational polynomial fit to the ellipsometric data.

and  $a_2 = 6.42$  eV (dashed line in Figure 2). The present ellipsometry measurements thus confirm the strong excitonic contribution to the dielectric function for polarization perpendicular to the *c*-axis.

**Figure 3** shows the electronic band structure of *h*-BN calculated within the *GW* approximation. A direct bandgap of 6.95 eV is found, in contrast with lower values of 4.6 eV obtained by density functional theory (DFT) in the local density approximation (LDA) or 6.19 eV in the  $G_0W_0$  quasiparticle

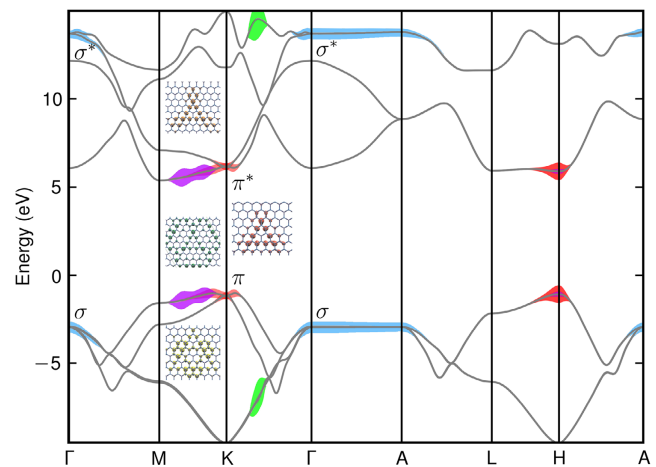


**Figure 3.** Electronic band structure of bulk *h*-BN calculated within the *GW* approximation. The shaded regions represent the electron–hole density of states that contribute to the excitonic excitations projected along the *h*-BN band structure. The exciton wave functions for the hole on a boron atom at the center are sketched: in the *K*– $\Gamma$  sector, for the lowest excitonic transition at 6.03 eV; in the *M*–*K* sector, from top to bottom, for the excitonic transitions at 6.69, 6.66, and 6.54 eV.

approximation. This trend is in good agreement with recent DFT and quasiparticle calculations reported on monolayer and bulk *h*-BN.<sup>[52]</sup> The first excitonic peak at  $\approx 6$  eV (see Figure 1) is due to the  $\pi \rightarrow \pi^*$  transitions that are strongly renormalized by excitonic effects. In Figure 3, the electron–hole pair density of states that make up the excitonic transition at  $\approx 6$  eV is projected along the *h*-BN band structure and displayed as red shaded areas. The exciton is primarily formed by electron–hole transitions close to the *K*(*H*) point. The calculated excitonic absorption peak at  $\approx 6$  eV agrees remarkably well with the experiment (see lower panel in Figure 1). Such good agreement may be a consequence of a partial cancellation between effects of the vibrational renormalization of the bandgap and the underestimation of the quasiparticle bandgap by the *GW* calculations, both of which have been estimated to be around 200–400 meV.<sup>[52,53]</sup>

Excitons in monolayer and few-layer *h*-BN have been analyzed in terms of Davydov multiplets,<sup>[54]</sup> revealing a structure in the imaginary part of the dielectric function that depends on the number of layers. A substantial increase in the direct bandgap and of the exciton binding energy was also reported in the monolayer owing to the reduction in screening.<sup>[54]</sup> In bulk *h*-BN, the lowest excitonic structures are composed of two pairs of degenerate peaks, which are split by interlayer interaction (Davydov splitting), the lowest pair being dark in linear response and bright in two-phonon absorption.<sup>[33,55]</sup> The other pair is formed by a combination of a bright and a dark exciton, and it is visible in linear response but is dark in two-phonon absorption.<sup>[55]</sup>

The calculations yield a weaker absorption peak around 6.6 eV which originates from electron–hole transitions along the *K*–*M* line. The projected electron–hole density of states contributing to this peak is shown in Figure 3 as shaded purple areas. The higher excitons that make up this peak are calculated to be at 6.54, 6.66, and 6.69 eV and their wave functions are shown in Figure 3. Some of the excitations correspond to higher excitations in

the monolayer<sup>[56,57]</sup> and other are specific to the bulk. The calculated peak at 6.6 eV agrees well with a weaker feature observed slightly above the direct bandgap at 6.82 eV in the imaginary part of the dielectric function derived from the ellipsometry measurements.

The strong peak at 15.23 eV that appears in the calculated absorption spectrum (see Figure 1) arises primarily from  $\sigma \rightarrow \sigma^*$  transitions around the  $\Gamma$  point. The projected electron-hole density of states contributing to these transitions is shown in Figure 3 as shaded blue areas. The flat dispersion of the electronic bands along the  $\Gamma$ -A line gives rise to a high density of states and contributes to the strong optical absorption of this excitonic transition. Early UV reflectivity measurements suggested a  $\sigma \rightarrow \sigma^*$  transition at a similar energy, although its origin was assigned to interband transitions near the  $M$  point<sup>[58]</sup> because of the lack of quasiparticle corrections in their band structure. Our ab initio calculations clearly indicate that the greatest contribution arises from wavevectors around the  $\Gamma$  point. At high energies, a strong absorption band at 15 eV is revealed by the ellipsometry measurements. While this band is substantially broadened in relation to the results of the theoretical calculations, its energy location agrees well with the ab initio calculations and can be assigned to the  $\sigma \rightarrow \sigma^*$  transitions discussed earlier. Other weak structures can be observed in the calculated imaginary part of the dielectric function at higher energies, around 19.0 and 20.5 eV. As shown in Figure 3, these features originate again from  $\sigma \rightarrow \sigma^*$  transitions, but in this case they involve bands located roughly at the mid  $K$ - $\Gamma$  line (green shaded areas) and  $A$ - $L$  line (not shown). In these regions, the joint density of states is very low, which explains the weak intensity of these peaks. A corresponding weak, broad band can be clearly observed at 19.2 eV in the imaginary part of the dielectric

function derived from the ellipsometry measurements. In general, spectroscopic features of the dielectric function at higher energies exhibit a significant broadening with respect to the theoretical predictions.

In the energy range between  $\approx 7$  and  $\approx 13$  eV, the sample is found to be transparent in the optical experiments. Therefore, and because our setup at the synchrotron is not equipped with an autoretarder, the resulting dielectric function is very noisy in this spectral range. The dielectric response of  $h$ -BN in the deep-UV region thus exhibits two transparency spectral regions. This is shown in **Figure 4**, where one can see that after the strong sharp absorption peak associated with the  $\pi \rightarrow \pi^*$  electronic transitions, a wide transparency region exists until the higher  $\sigma \rightarrow \sigma^*$  transitions give rise to a sizable optical absorption. This behavior follows from the  $h$ -BN band structure, in which the higher (lower) conduction (valence) bands located between those involved in the  $\pi \rightarrow \pi^*$  and  $\sigma \rightarrow \sigma^*$  transitions responsible for the dominant absorption peaks display dissimilar and often opposite gradients, thus leading to very low joint density of states for the optical transitions. Therefore, from ellipsometry measurements up to 25 eV, we have identified two wide transparency regions in  $h$ -BN: one region in the IR-UV spectral range and another region located in the deep-UV between 7 and 13 eV. The UV-light penetration depth varies strongly across the measured spectral range. At 5 eV, in the transparency region below the main excitonic absorption peak, the penetration depth is 73 nm, whereas it is only 0.8 nm at the absorption peak at 6.12 eV. In the transparency window beyond the main excitonic peak, it reaches a maximum of 38 nm at 8.5 eV and then decreases again to 0.8 nm at the second absorption peak at 15 eV. From there on, the penetration depth in the far-UVC is consistently low (less than 2 nm up to 20 eV).

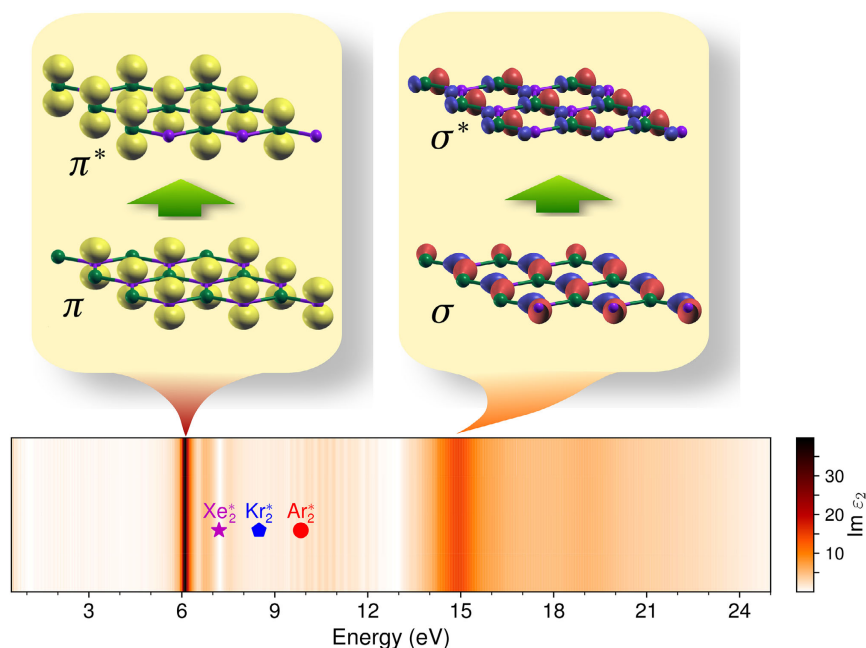


**Figure 4.** Transparency window in  $h$ -BN between the fundamental bandgap absorption driven by  $\pi \rightarrow \pi^*$  transitions and the higher bandgap absorption driven by  $\sigma \rightarrow \sigma^*$  transitions. The symbols indicate the emission energies of the most commonly used deep-UV excimer lamps (from ref. [11]). In the sketch of the orbitals, green balls represent boron atoms and purple balls represent nitrogen atoms.

### 3. Conclusions

We have conducted a detailed ellipsometric study of *h*-BN over an extended energy range up to 25 eV using synchrotron radiation. This is the first ellipsometric study performed with synchrotron radiation in 2D/layered compounds. The ordinary dielectric function  $\epsilon_{\perp}$  has been determined by point-by-point fitting of the ellipsometry data. A dominant contribution at 6.12 eV corresponding to the direct bandgap  $\pi \rightarrow \pi^*$  transitions at  $K(H)$  yields a sharp absorption peak. A second peak at 6.82 eV has been observed and assigned to  $\pi \rightarrow \pi^*$  transitions along the  $M-K$  line. The dispersion of the ordinary refractive index for below bandgap energies is in excellent agreement with previous determinations based on transmission experiments. The steep increase in the refractive index as the bandgap is approached is an indication of the huge excitonic effects in *h*-BN and is consistent with the  $GW+$  Bethe–Salpeter equation (BSE) calculations presented.

At higher energies, a second strong absorption peak is found at 15 eV. According to our *ab initio* calculations, this peak is well accounted for by  $\sigma \rightarrow \sigma^*$  transitions around the  $\Gamma$  point, although the ellipsometric data yield a broader and weaker peak than predicted by the calculations. Another weaker structure at about 19.2 eV has been observed in the ellipsometry measurements, which, according to the calculated band structure, can be assigned to electronic interband transitions along the  $\Gamma-L$  line.

The good agreement between the ellipsometry results and the  $GW+$  BSE calculations substantiates the accuracy of the self-consistent  $GW$  framework for an adequate description of the electronic structure of *h*-BN, and widens our knowledge of higher energy electronic transitions in this highly topical ultrawide bandgap material.

*h*-BN has been shown to be a singular van der Waals crystal that exhibits a further gap in the far-UVC beyond the fundamental bandgap energy. A wide transparency window between  $\approx 7$  and  $\approx 13$  eV has been found from the ellipsometry measurements. This transparency window lies in a spectral range that is relevant for far-UVC present-day technological applications in disinfection, waste treatment, and ultrahigh resolution lithography, and may be useful for future device development operating in the far-UVC spectral range.

### 4. Experimental Section

High-quality *h*-BN single-crystal samples were grown by using the metal-flux method, with 50 wt% Ni and 50 wt% Cr mixtures with a hot-pressed *h*-BN ceramic crucible, which also served as the source material. The furnace was evacuated and then filled with a continuous flow of  $N_2$  and forming gas to a pressure of 850 Torr, to minimize oxygen and carbon impurities. After a dwell time of 24 h at 1550 °C, the *h*-BN crystals were precipitated by cooling at a rate of  $1\text{ }^{\circ}\text{C h}^{-1}$  to 1550 °C, and then the system was rapidly quenched to room temperature. The selected sample for synchrotron ellipsometry had lateral dimensions on the order of 1–2 mm and a very smooth surface.

The high quality of these *h*-BN crystals has been verified by several techniques. The crystals are highly oriented with the [0001] axis perpendicular to the sample surface, as determined by X-ray diffraction.<sup>[59]</sup> The root mean square surface roughness over a  $2\text{ }\mu\text{m} \times 2\text{ }\mu\text{m}$  area was 0.4 nm, as measured by atomic force microscopy (AFM). Over a wider area, terraces may occur in *h*-BN samples,<sup>[60]</sup> which may lead to an increased apparent roughness. The Raman  $E_{2g}^{\text{high}}$  peak widths for these *h*-BN crystals are narrow, with room temperature values of  $7.5\text{ cm}^{-1}$ .<sup>[40,42]</sup> X-ray photoelectron

spectroscopy detected only boron and nitrogen.<sup>[60]</sup> The low-temperature photoluminescence spectra have multiple narrow phonon replicas above 5.75 eV which are only present in high-quality *h*BN.<sup>[61]</sup> Transmission electron microscopy (TEM) measurements revealed the formation of etch pits where dislocations intersect the surface, with an etch pit density of  $5\text{ }10\text{ cm}^{-2}$ , upon defect sensitive etching on *h*-BN crystals grown by this technique.<sup>[62]</sup>

Spectroscopic ellipsometry was performed using two different instruments. For the energy region up to 6.5 eV, a commercial variable-angle ellipsometer (Woollam VASE) was used. This instrument is equipped with an autoretarder, which allows one to accurately access transparent regions of the sample. Ellipsometric parameters  $\Psi$  and  $\Delta$  were acquired at three angles of incidence ( $50^{\circ}$ ,  $60^{\circ}$ , and  $70^{\circ}$ ) in steps of 10 meV. The system has a circular light spot of about 3–4 mm in diameter. For slanted angles required in ellipsometry, the area under illumination enlarges and straddles sample edges in the case of small samples like the one investigated here.

At photon energies higher than 5 eV, a synchrotron-based home-built spectroscopic ellipsometer was used at the Metrology Light Source (MLS) of the Physikalisch Technische Bundesanstalt (PTB) synchrotron in Berlin, Germany. In contrast with the laboratory setup, the synchrotron beam has a circular shape with a spot size of less than 1 mm in diameter, and therefore it is possible to keep it fully on the sample surface even at a slanted incidence. However, several alignment steps at different photon energies are required at the synchrotron when optical elements such as gratings or filters are placed or removed from the optical path. These different alignments can lead to slight differences in the sample spot under study. However, the sample under investigation is the same for both instruments and to the best of our abilities we performed alignments on the very same spot. The measurements in the spectral range up to 25 eV were covered in two different runs. Between 5 and 9.5 eV, steps of 10 meV were selected, while for a second experiment between 9.5 and 25 eV, the step size was increased to 50 meV. Both experiments were performed at the same angle of incidence of  $67^{\circ}$  to minimize calibration errors between the two runs. More details about the experimental setup can be found elsewhere.<sup>[63]</sup> The sample was carefully mounted on a vacuum compatible glue pad for both experimental setups. Because the optical axis of the sample is oriented perpendicular to the surface, we are only able to investigate the ordinary tensor component of the dielectric function of the highly anisotropic *h*-BN crystal.<sup>[44]</sup> To obtain the dielectric function from the ellipsometric data, we first looked at the transparency region below 5 eV and modeled the refractive index behavior by assuming the extraordinary dielectric function from the study by Segura et al.<sup>[44]</sup> The resulting ordinary dielectric function agrees well with the result reported in the study by Segura et al.,<sup>[44]</sup> as shown in Figure 2, where both determinations are compared. Higher photon energy regions were analyzed exclusively in the isotropic approximation<sup>[64,65]</sup> without making any assumption about the extraordinary tensor component. Only the thickness of a top Bruggeman effective-medium layer to account for surface roughness was adjusted.<sup>[66]</sup> The best results are obtained for an effective-medium layer thickness of 0.5 nm, in good agreement with AFM characterization.

A point-by-point fitted dielectric function was obtained by numerical inversion of the ellipsometric angles  $\Psi$  and  $\Delta$ , taking into account the surface roughness in the Bruggeman effective-medium approximation and the angles of incidence. To facilitate the analysis, this point-by-point fitting scheme was applied for the different energy ranges of the specific instrument runs separately. Therefore, the final dielectric function still suffers from noise particularly in the 9–13 eV range, but a continuous connected line shape is obtained as results from other energy ranges are provided as additional input for each energy region. Fits to the  $\Psi$  and  $\Delta$  ellipsometric data in the different regions and further discussion of the fitting procedure are given in the Supporting Information. The whole fitting process was iteratively repeated till convergence was achieved. The obtained point-by-point fitted dielectric function was then used to create an oscillator model from Kramers–Kronig consistent analytic oscillator functions which are used to empirically model the result. The comparison of this result with our point-by-point fit serves as a control

for the Kramers–Kronig consistency of this approach, and at the same time it corroborates our choice of 0.5 nm thickness for the surface roughness layer.

Starting with the independent-particle band structure in the DFT and LDA,<sup>[67]</sup> the quasiparticle band structure was calculated within a GW scheme, with self-consistency on both the *G* and *W* eigenvalues.<sup>[68]</sup> The lattice parameters in our calculations are  $a = 2.496 \text{ \AA}$  and  $c = 6.610 \text{ \AA}$ . The computation of the dielectric function was performed using a  $24 \times 24 \times 6$  *k*-point grid, with 280 bands and a cutoff energy of 7 Ha. The optical absorption spectrum was calculated using the BSE<sup>[69]</sup> using 7 valence and 10 conduction bands. The full GW correction was calculated for these bands, while higher bands were rigidly shifted. For the analysis of the high energy excitons ( $E \geq 15$  eV), a  $12 \times 12 \times 4$  *k*-point grid was used to reduce computational demands to a feasible level.

## Supporting Information

Supporting Information is available from the Wiley Online Library or from the author.

## Acknowledgements

This work was supported by the Spanish MINECO/FEDER under grant no. MAT2015-71035-R. The authors thank Norbert Esser (Leibniz Institut für Analytische Wissenschaften – ISAS-e.V.) for access to the synchrotron ellipsometer and the PTB (Physikalisch Technische Bundesanstalt) for expert assistance during the beamtime at the MLS synchrotron. The authors gratefully acknowledge Michael Winkler (OvGU Magdeburg) for data recording at the synchrotron. C.A. acknowledges funding from the European Union Seventh Framework Program under grant agreement no. 785219 Graphene Core 2 and COST Action TUMIEE CA17126. C.A. acknowledges A. Saul for the management of the computer cluster Rosa. Support for the *h*-BN crystal growth from the Office of Naval Research award number N00014-20-1-2474 is appreciated. The authors thank Dr. Neelam Khan (Georgia Gwinnett College) for the AFM analysis.

## Conflict of Interest

The authors declare no conflict of interest.

## Data Availability Statement

Research data are not shared.

## Keywords

2D layered materials, electronic structure, far-UVC, spectroscopic ellipsometry

Received: October 19, 2020

Revised: January 20, 2021

Published online: March 10, 2021

- 
- [1] K. Song, M. Mohseni, F. Taghipour, *Water Res.* **2016**, *94*, 341.  
 [2] S. J. Pearton, D. P. Norton, F. Ren, *Metal Oxide Nanomaterials for Chemical Sensors*, Springer, New York **2012**, pp. 321–343.  
 [3] M. Honda, Y. Kumamoto, A. Taguchi, Y. Saito, S. Kawata, *Appl. Phys. Lett.* **2014**, *104*, 061108.  
 [4] C. Pernot, A. Hirano, M. Iwaya, T. Detchprohm, H. Amano, I. Akasaki, *Jpn. J. Appl. Phys.* **2000**, *39*, L387.  
 [5] R. J. Drost, B. M. Sadler, *Semicond. Sci. Technol.* **2014**, *29*, 084006.

- [6] X. Sun, W. Cai, O. Alkhazragi, E.-N. Ooi, H. He, A. Chaaban, C. Shen, H. M. Oubei, M. Z. M. Khan, T. K. Ng, M.-S. Alouini, B. S. Ooi, *Opt. Express* **2018**, *26*, 12870.  
 [7] D. Welch, M. Buonanno, V. Grilj, I. Shuryak, C. Crickmore, A. W. Bigelow, G. Randers-Pehrson, G. W. Johnson, D. J. Brenner, *Sci. Rep.* **2018**, *8*, 2752.  
 [8] ISO 21348:2007, International Organization for Standardization, <https://www.iso.org/standards.html> (accessed: July 2020).  
 [9] M. Buonanno, D. Welch, I. Shuryak, D. J. Brenner, *Sci. Rep.* **2020**, *10*, 10285.  
 [10] International Commission on Non-Ionizing Radiation Protection, UVC lamps and SARS-COV-2, <https://www.icnirp.org/en/activities/news/news-article/sars-cov-2-and-uvc-lamps.html> (accessed: July 2020).  
 [11] X. Xu, *Thin Solid Films* **2001**, *390*, 237.  
 [12] G. Heit, A. Neuner, P.-Y. Saugy, A. M. Braun, *J. Phys. Chem. A* **1998**, *102*, 5551.  
 [13] T. Oppenländer, S. Gliese, *Chemosphere* **2000**, *40*, 15.  
 [14] Q.-R. Li, C.-Z. Gu, Y. Di, H. Yin, J.-Y. Zhang, *J. Hazard. Mater.* **2006**, *133*, 68.  
 [15] F. Bauer, U. Decker, K. Czihal, R. Mehnert, C. Riedel, M. Riemschneider, R. Schubert, M. R. Buchmeiser, *Prog. Org. Coat.* **2009**, *64*, 474.  
 [16] A. Takakuwa, M. Ikawa, M. Fujita, K. Yase, *Jpn. J. Appl. Phys.* **2007**, *46*, 5960.  
 [17] T. Mukai, M. Yamada, S. Nakamura, *Jpn. J. Appl. Phys.* **1999**, *38*, 3976.  
 [18] M. Kneissl, T.-Y. Seong, J. Han, H. Amano, *Nat. Photonics* **2019**, *13*, 233.  
 [19] T. Takano, T. Mino, J. Sakai, N. Noguchi, K. Tsubaki, H. Hirayama, *Appl. Phys. Express* **2017**, *10*, 031002.  
 [20] Z. Zhang, M. Kushimoto, T. Sakai, N. Sugiyama, L. J. Schowalter, C. Sasaoka, H. Amano, *Appl. Phys. Express* **2019**, *12*, 124003.  
 [21] B. K. SaifAddin, A. S. Almogbel, C. J. Zollner, F. Wu, B. Bonef, M. Iza, S. Nakamura, S. P. DenBaars, J. S. Speck, *ACS Photonics* **2020**, *7*, 554.  
 [22] S. J. Pearton, J. Yang, P. H. Cary, F. Ren, J. Kim, M. J. Tadjer, M. A. Mastro, *Appl. Phys. Rev.* **2018**, *5*, 011301.  
 [23] *Gallium Oxide: Technology, Devices and Applications* (Eds: S. Pearton, F. Ren, M. Mastro), Elsevier, Amsterdam/New York **2019**.  
 [24] A. Segura, L. Artús, R. Cuscó, R. Goldhahn, M. Feneberg, *Phys. Rev. Mater.* **2017**, *1*, 024604.  
 [25] M. Feneberg, J. Nixdorf, M. D. Neumann, N. Esser, L. Artús, R. Cuscó, T. Yamaguchi, R. Goldhahn, *Phys. Rev. Mater.* **2018**, *2*, 044601.  
 [26] K. Watanabe, T. Taniguchi, H. Kanda, *Nat. Mater.* **2004**, *3*, 404.  
 [27] K. Watanabe, T. Taniguchi, T. Niiyama, K. Miya, M. Taniguchi, *Nat. Photonics* **2009**, *3*, 591.  
 [28] J. D. Caldwell, I. Aharonovich, G. Cassabo, J. H. Edgar, B. Gil, D. N. Basov, *Nat. Rev. Mater.* **2019**, *4*, 552.  
 [29] A. Hussain, C. Gautam, A. Jafri, V. K. Mishra, A. Madheshiya, A. Gautam, M. K. Singh, R. K. Gautam, M. Gupta, M. Arshad, R. Vajtai, P. M. Ajayan, *Ceram. Int.* **2020**, *46*, 23006.  
 [30] B. Arnaud, S. Lebègue, P. Rabiller, M. Alouani, *Phys. Rev. Lett.* **2006**, *96*, 026402.  
 [31] E. Cannuccia, B. Monserrat, C. Attacalite, *Phys. Rev. B* **2019**, *99*, 081109(R).  
 [32] X. Blase, A. Rubio, S. G. Louie, M. L. Cohen, *Phys. Rev. B* **1995**, *51*, 6868.  
 [33] G. Cassabo, P. Valvin, B. Gil, *Nat. Photonics* **2016**, *10*, 262.  
 [34] T. Q. P. Vuong, G. Cassabo, P. Valvin, V. Jacques, R. Cuscó, L. Artús, B. Gil, *Phys. Rev. B* **2017**, *95*, 045207.  
 [35] F. Paleari, H. P. Miranda, A. Molina-Sánchez, L. Wirtz, *Phys. Rev. Lett.* **2019**, *122*, 187401.  
 [36] L. Schué, L. Sponza, A. Plaud, H. Bensalah, K. Watanabe, T. Taniguchi, F. Ducastelle, A. Loiseau, J. Barjon, *Phys. Rev. Lett.* **2019**, *122*, 067401.

- [37] J. D. Caldwell, A. V. Kretinin, Y. Chen, V. Giannini, M. M. Fogler, Y. Francescato, C. T. Ellis, J. G. Tischler, C. R. Woods, A. J. Giles, M. Hong, K. Watanabe, T. Taniguchi, S. A. Maier, K. S. Novoselov, *Nat. Commun.* **2014**, *5*, 5221.
- [38] A. J. Giles, S. Dai, I. Vurgaftman, T. Hoffman, S. Liu, L. Lindsay, C. T. Ellis, N. Assefa, I. Chatzakis, T. L. Reinecke, J. G. Tischler, M. M. Fogler, J. H. Edgar, D. N. Basov, J. D. Caldwell, *Nat. Mater.* **2017**, *17*, 134.
- [39] R. Cuscó, B. Gil, G. Cassabois, L. Artús, *Phys. Rev. B* **2016**, *94*, 155435.
- [40] R. Cuscó, L. Artús, J. H. Edgar, S. Liu, G. Cassabois, B. Gil, *Phys. Rev. B* **2018**, *97*, 155428.
- [41] R. Cuscó, J. H. Edgar, S. Liu, G. Cassabois, B. Gil, L. Artús, *Phys. Rev. B* **2019**, *99*, 085428.
- [42] R. Cuscó, J. H. Edgar, S. Liu, J. Li, L. Artús, *Phys. Rev. Lett.* **2020**, *124*, 167402.
- [43] R. Cuscó, J. Pellicer-Porres, J. H. Edgar, J. Li, A. Segura, L. Artús, *Phys. Rev. B* **2020**, *102*, 075206.
- [44] A. Segura, L. Artús, R. Cuscó, T. Taniguchi, G. Cassabois, B. Gil, *Phys. Rev. Mater.* **2018**, *2*, 024001.
- [45] A. Segura, R. Cuscó, T. Taniguchi, K. Watanabe, G. Cassabois, B. Gil, L. Artús, *J. Phys. Chem. C* **2019**, *123*, 17491.
- [46] A. Segura, R. Cuscó, T. Taniguchi, K. Watanabe, L. Artús, *Phys. Rev. B* **2020**, *101*, 235203.
- [47] M. Kolos, F. Karlický, *Phys. Chem. Chem. Phys.* **2019**, *21*, 3999.
- [48] V. G. Kravets, A. N. Grigorenko, R. R. Nair, P. Blake, S. Anissimova, K. S. Novoselov, A. K. Geim, *Phys. Rev. B* **2010**, *81*, 155413.
- [49] Y. Panayiotatos, S. Logothetidis, A. Laskarakis, A. Zervopoulou, M. Gioti, *Diamond Relat. Mater.* **2002**, *11*, 1281.
- [50] M. A. McKay, J. Li, J. Y. Lin, H. X. Jiang, *J. Appl. Phys.* **2020**, *127*, 053103.
- [51] D. Hahn, *Opt. Photonik* **2014**, *9*, 45.
- [52] R. J. Hunt, B. Monserrat, V. Zólyomi, N. D. Drummond, *Phys. Rev. B* **2020**, *101*, 205115.
- [53] T. Shen, X.-W. Zhang, H. Shang, M.-Y. Zhang, X. Wang, E.-G. Wang, H. Jiang, X.-Z. Li, *Phys. Rev. B* **2020**, *102*, 045117.
- [54] F. Paleari, T. Galvani, H. Amara, F. Ducastelle, A. Molina-Sánchez, L. Wirtz, *2D Mater.* **2018**, *5*, 045017.
- [55] C. Attacalite, M. Grüning, H. Amara, S. Latil, F. Ducastelle, *Phys. Rev. B* **2018**, *98*, 165126.
- [56] T. Galvani, F. Paleari, H. P. C. Miranda, A. Molina-Sánchez, L. Wirtz, S. Latil, H. Amara, F. Ducastelle, *Phys. Rev. B* **2016**, *94*, 125303.
- [57] W. Aggoune, C. Cocchi, D. Nabok, K. Rezouali, M. A. Belkhir, C. Draxl, *Phys. Rev. B* **2018**, *97*, 241114.
- [58] R. Mamy, J. Thomas, G. Jezequel, J. Lemonnier, *J. Phys. Lett.* **1981**, *42*, 473.
- [59] T. Hoffman, B. Clubine, Y. Zhang, K. Snow, J. Edgar, *J. Cryst. Growth* **2014**, *393*, 114.
- [60] S. Liu, R. He, L. Xue, J. Li, B. Liu, J. H. Edgar, *Chem. Mater.* **2018**, *30*, 6222.
- [61] T. Q. P. Vuong, S. Liu, A. van de Lee, R. Cuscó, L. Artús, T. Michel, P. Valvin, J. H. Edgar, G. Cassabois, B. Gil, *Nat. Mater.* **2018**, *17*, 152.
- [62] J. H. Edgar, S. Liu, T. Hoffman, Y. Zhang, M. E. Twigg, N. D. Bassim, S. Liang, N. Khan, *J. Appl. Phys.* **2017**, *122*, 225110.
- [63] M. D. Neumann, C. Cobet, H. Kaser, M. Kolbe, A. Gottwald, M. Richter, N. Esser, *Rev. Sci. Instrum.* **2014**, *85*, 055117.
- [64] D. E. Aspnes, *J. Opt. Soc. Am.* **1980**, *70*, 1275.
- [65] S. Zollner, J. G. Chen, E. Duda, T. Wetteroth, S. R. Wilson, J. N. Hilfiker, *J. Appl. Phys.* **1999**, *85*, 8353.
- [66] D. A. G. Bruggeman, *Ann. Phys.* **1935**, *416*, 636.
- [67] P. Giannozzi, S. Baroni, N. Bonini, M. Calandra, R. Car, C. Cavazzoni, D. Ceresoli, G. L. Chiarotti, M. Cococcioni, I. Dabo, A. D. Corso, S. de Gironcoli, S. Fabris, G. Fratesi, R. Gebauer, U. Gerstmann, C. Gougoussis, A. Kokalj, M. Lazzeri, L. Martin-Samos, N. Marzari, F. Mauri, R. Mazzarello, S. Paolini, A. Pasquarello, L. Paulatto, C. Sbraccia, S. Scandolo, G. Sclauzero, A. P. Seitsonen, et al., *J. Phys.: Condens. Matter* **2009**, *21*, 395502.
- [68] D. Sangalli, A. Ferretti, H. Miranda, C. Attacalite, I. Marri, E. Cannuccia, P. Melo, M. Marsili, F. Paleari, A. Marrazzo, G. Prandini, P. Bonfà, M. O. Atambo, F. Affinito, M. Palumbo, A. Molina-Sánchez, C. Hogan, M. Grüning, D. Varsano, A. Marini, *J. Phys.: Condens. Matter* **2019**, *31*, 325902.
- [69] G. Strinati, *Riv. Nuovo Cimento* **1988**, *11*, 1.